Colloids and Surfaces B: Biointerfaces 261 (2026) 115417

Contents lists available at ScienceDirect

Colloids and Surfaces B: Biointerfaces

journal homepage: www.elsevier.com/locate/colsurfb

Conformal polypyrrole biointerfaces on porous PHA monoliths via oxidative chemical vapor deposition

Adriana Kovalcik [a,*], Nicole Cernekova [a], Fika Fauzi [b], Ranjita K. Bose [b], Zdenko Spitalsky [c], Zuzana Kadlecova [d], Lucy Vojtova [a,d], Zdenka Víchová [e], Petr Humpolíček [e], Patrycja Bober [f]

[a] *Faculty of Chemistry, Brno University of Technology, Brno 612 00, Czech Republic*
[b] *Engineering and Technology Institute Groningen, University of Groningen, Nijenborgh 3, Groningen 9747AG, the Netherlands*
[c] *Polymer Institute, Slovak Academy of Sciences, Dubravska Cesta 9, Bratislava 845 41, Slovak Republic*
[d] *CEITEC – Central European Institute of Technology, Brno University of Technology, Purkynova 123, Brno 612 00, Czech Republic*
[e] *Centre of Polymer Systems, Tomas Bata University in Zlin, Tř. T . Bati 5678, Zlin 760 01, Czech Republic*
[f] *Institute of Macromolecular Chemistry, Czech Academy of Sciences, Prague 162 00, Czech Republic*

ARTICLE INFO

Keywords:
Polyhydroxyalkanoates
Polypyrrole
Oxidative chemical vapor deposition
Porous monolith
Biointerface
Wound dressing

ABSTRACT

Chronic wounds require dressings that manage exudate, conform to soft tissue, provide mechanical support, and deliver intrinsic bioactivity. Here, we report conductive, hydrogel-like porous polyhydroxyalkanoate (PHA) monoliths dressings coated with polypyrrole (PPy) using oxidative chemical vapor deposition (oCVD). Porous PHA substrates were prepared from polyhydroxybutyrate (PHB) and a P4HB-containing copolymer by thermally induced phase separation and were uniformly functionalized throughout their three-dimensional architecture by this solvent-free process. The resulting PHA/PPy porous monoliths combine high water uptake with electrical conductivity and biological activity. They exhibit a swelling ratio of ~250 %, maintaining a moist environment while preserving viscoelastic integrity. Sheet resistance ranges from 26 to 86 kΩ/sq, enabling platforms for electrical sensing in tissue repair. The composites do not induce cytotoxicity and exhibit intrinsic radical-scavenging capacity and antibacterial activity against both *Gram-positive* and *Gram-negative* bacteria. These properties are achieved without chemical derivatization of the PHA matrix. The hydrophobic PHA core provides mechanical robustness, while the conformal PPy layer imparts conductivity and bioactivity. Overall, this oCVD route provides a scalable, solvent-free strategy to engineer multifunctional, hydrogel-like porous monolith dressings that integrate moisture management, mechanical resilience, electrical conduction, and inherent antioxidant and antimicrobial activity. These features position the developed materials as promising bioactive and bioelectronic wound dressings and soft tissue interfaces.

1. Introduction

Chronic wounds remain difficult to treat because their pathophysiology is multifactorial and complications are frequent [1]. Chronic ulcers such as diabetic foot ulcers, pressure ulcers, and venous leg ulcers often do not progress through the normal stages of healing [2,3]. Despite standard measures such as wound offloading, infection control, debridement, and glycemic management, reinfection, biofilm formation, and delayed healing are common [1,4]. Consequently there is a need for dressings that manage exudate, match the viscoelastic behaviour of soft tissue, conform to irregular wound beds, and provide intrinsic antibacterial and antioxidant activity [4].

Hydrogels can mimic extracellular matrix, support cellular interactions, and maintain a moist environment due to high water content [5–7]. Their main limitation is low mechanical strength and a strong dependence of viscoelastic response on polymer composition, crosslinking, and water content [8]. To overcome these limits, strategies such as double network design, nanocomposite reinforcement, fibre reinforcement, dynamic covalent chemistry, and three-dimensional printing have been introduced, but they often bring trade–offs in biocompatibility or process complexity [9–11].

Polyhydroxyalkanoates are biotechnologically produced

---

[*] Correspondence to: Faculty of Chemistry, BrnoUniversity of Technology, Purkynova 118, Brno 612 00, Czech Republic.
E-mail address: kovalcik@fch.vut.cz (A. Kovalcik).

https://doi.org/10.1016/j.colsurfb.2026.115417
Received 27 August 2025; Received in revised form 22 December 2025; Accepted 5 January 2026

thermoplastics with good biocompatibility and tunable mechanics [12–14]. They are promising for regenerative medicine and wound care, yet they are inherently hydrophobic and do not form hydrogels. Hydrophilicity can be increased by chemical modification such as sulfonation or carboxylation, but this adds synthesis steps and can alter biological response [15,16]. An alternative is morphological and compositional control of the polymer. Thermally induced phase separation enables porous monoliths with interconnected pores and transport pathways for water and cells [17]. Selecting the copolymer poly (3-hydroxybutyrate-co-4-hydroxybutyrate) and blending with poly (3-hydroxybutyrate) reduces crystallinity and improves toughness and flexibility, which facilitates processing and water interaction [18,19].

Electrical cues represent another important strategy in wound care. Conducting polymers such as polypyrrole (PPy) are attractive in this context because they combine electrical conduction with redox activity and can provide intrinsic antibacterial effects, making them promising components of bioactive and bioelectronic wound dressings. Electrical stimulation and conductive surfaces can support cell proliferation, tissue regeneration, and healing [20]. Conductive hydrogels and related materials are commonly produced either by adding conductive fillers that create percolation pathways or by integrating conducting polymers that provide uniform conductivity and biological interaction [21]. Conducting polymers are often preferred in biomedical contexts for their continuous conductive phase, compatibility with soft matrices, and capacity for interfacial interaction with cells [22–25]. Polypyrrole is especially attractive because it combines electrical function with documented antioxidant and antibacterial behaviour and with encouraging biocompatibility when appropriately formulated [22,26–28].

A key challenge is to form thin and conformal conductive layers inside architected porous bodies without solvents that could affect PHA integrity. Oxidative chemical vapor deposition is an all–dry method that produces conformal conducting polymer coatings on three-dimensional substrates under mild conditions [30,31]. Recent studies clarified growth mechanisms and electrochemical performance of oCVD polypyrrole on substrates such as glass, fibres, and carbon fabric mainly for optoelectronic and energy applications, yet translation to porous PHA bodies for biointerfaces has not been established [32,33].

Here we combine thermally induced phase separation and blending of poly(3-hydroxybutyrate) with poly(3-hydroxybutyrate-co-4-hydroxybutyrate) to produce porous PHA monoliths, and we apply oxidative chemical vapor deposition to deposit conformal PPy throughout their three-dimensional architecture. We hypothesize that this solvent-free route yields hydrogel-like porous monolith dressings that integrate moisture management, mechanical resilience, electrical functionality, and intrinsic antibacterial and antioxidant behaviour while maintaining cytocompatibility. The goals are to establish feasibility of oCVD on solvent–sensitive PHA substrates, to relate morphology to coating quality, and to evaluate antioxidant, antibacterial, and cytocompatible performance in the context of bioactive and bioelectronic wound dressings. This work addresses the lack of a solvent-free route to conformal conducting polymer coatings inside solvent–sensitive PHA porous monoliths that deliver hydrogel–like swelling without chemical modification while retaining biointerface function.

2. Experimental section

2.1. Materials

Poly(3-hydroxybutyrate) (P3HB, grade P338, Mn = 206 ± 0.007 kg mol^{-1}) was sourced from Biomer GmbH (Schwalbach, Germany). The copolymer poly(3-hydroxybutyrate-co-4-hydroxybutyrate) [P(3HB-co-4HB), Mirel type, Mn = 144 ± 0.005 kg mol^{-1}] was obtained from Telles Inc. (Lowell, MA, USA). Dimethyl sulfoxide (DMSO, analytical grade) was purchased from Lach-Ner s.r.o. (Neratovice, Czech Republic). Pyrrole monomer (≥ 99 %) was supplied by TCI Europe N.V. (Zwijndrecht, Belgium). Antimony pentachloride ($SbCl_5$, > 98 %), hydrochloric acid (HCl, 37 %), potassium chloride (KCl, > 99.5 %), and potassium hydroxide (KOH, 99.99 %) were all acquired from Sigma-Aldrich (St. Louis, MO, USA) and used without further purification. Silicon wafers were provided by Siegert Wafer GmbH (Aachen, Germany). For the cytotoxicity assay, Dulbecco's Modified Eagle Medium (DMEM, medium glucose), fetal bovine serum (FBS), penicillin/streptomycin, trypsin/EDTA, 2,3-bis-(2-methoxy-4-nitro-5-sulfophenyl)-2H-tetrazolium-5-carboxanilide (XTT sodium salt), and N-methyl dibenzopyrazine methyl sulfate (PMS) were purchased from Sigma Aldrich (USA).

2.2. Preparation of hydrogel-like porous monoliths

Porous PHA–based monoliths were prepared by thermally induced phase separation with slight modifications [17]. Two types of monoliths were fabricated, one from neat poly(3-hydroxybutyrate) and one from a blend of poly(3-hydroxybutyrate) and poly (3-hydroxybutyrate-co-4-hydroxybutyrate). For the neat P3HB route, 600 mg of P3HB was dissolved in 6 mL of dimethyl sulfoxide by stirring at 80 °C for 5 min. The clear solution was poured into a cylindrical mold of 4 cm diameter and allowed to cool to room temperature to form a stiff organogel, which turned opaque over 24 h. The organogel was then washed with deionized water by solvent exchange at least five times over two days. Finally, the sample was lyophilized to obtain a dry porous monolith of approximately 2.3 mm thickness, hereafter designated PHB_S.

The blend route followed the same protocol using a 1–1 mass mixture of P3HB and P(3HB-co-4HB) with 300 mg of each polymer dissolved in 6 mL of dimethyl sulfoxide. After gelation, solvent exchange, and lyophilization, the resulting porous monolith is referred to as PHA_S.

2.3. Deposition of polypyrrole by oxidative chemical vapor deposition

Porous monoliths PHB_S and PHA_S were coated with PPy using oxidative chemical vapor deposition (oCVD). This solvent-free vapor phase method enables simultaneous polymerisation and doping of pyrrole directly on the sample surface, yielding a uniform and conformal conductive PPy layer. The process was adapted from Fauzi et al., 2024 with adjustments for porous biopolymer substrates [31,34]. Because oCVD PPy forms an insoluble, partially crosslinked thin film, its conventional number- and weight-average molecular weights cannot be determined by solution-based methods (e.g. SEC/GPC or viscometry). Therefore, the deposition parameters used here were selected based on effective conjugation coordinate (ECC) analysis from our previous work, which correlates with PPy conjugation length and structural order [32].

Pyrrole monomer and antimony pentachloride oxidant were introduced into a temperature-controlled reactor in the vapor phase. The monomer and oxidant sources were held at 80 °C and 60 °C, respectively, and delivered at flow rates of 2.5 sccm for pyrrole and 0.5 sccm for antimony pentachloride, maintaining an oxidant-to- monomer flow ratio of 0.2. Nitrogen at 20 sccm served as the oxidant carrier. The reactor chamber was maintained at 300 mTorr and 40 °C, with the sample stage also at 40 °C to promote uniform deposition. The oxidant and monomer inlets were positioned orthogonally to minimize premature polymerisation.

To examine the effects of sample placement in the chamber (front or back) and deposition time (5 or 10 min) on coating performance, five circular samples of 15 mm diameter were mounted perpendicular to the oxidant flow and parallel with the monomer flow as depicted in Fig. 1. Final designations were PHB_S/PPy5 and PHB_S/PPy10 for the poly(3-hydroxybutyrate) monoliths and PHA_S/PPy5 and PHA_S/PPy10 for the blend monoliths, corresponding to 5 or 10 min deposition times.

After deposition, coated monoliths were stored under vacuum overnight to remove volatile species. A subset of PPy-coated samples was then immersed in absolute ethanol at room temperature for 24 h; the solvent remained colourless and no visible changes in sample

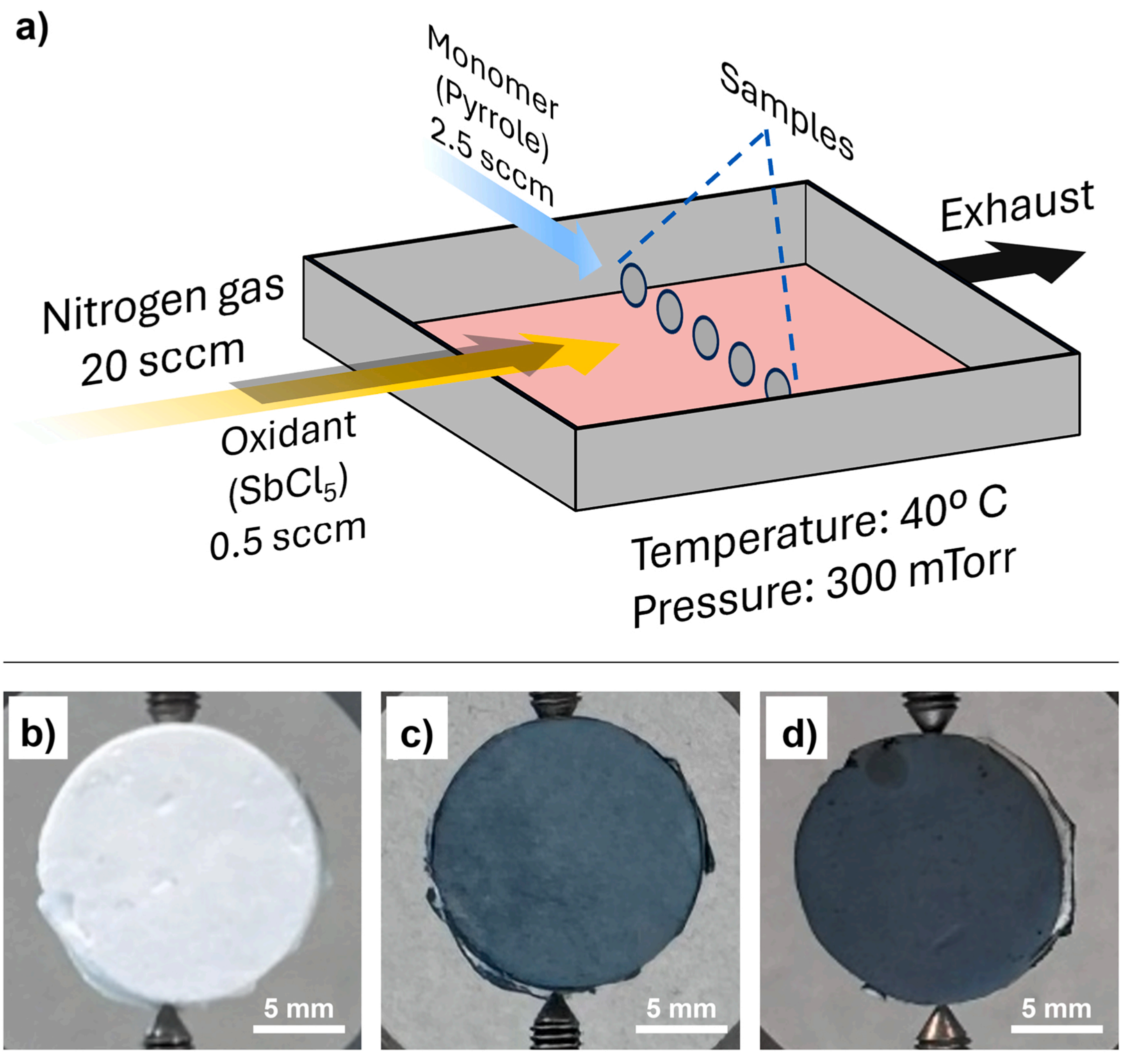

Fig. 1. (a) Schematic of the oxidative chemical vapor deposition (oCVD) setup used to deposit polypyrrole (PPy) on porous PHA monoliths, employing pyrrole as the monomer, $SbCl_5$ as the oxidant, and N_2 as the carrier gas (2.5, 0.5, and 20 sccm, respectively; 40 °C, 300 mTorr). Photographs of (b) neat PHB_S monolith before coating, (c) PHB_S/PPy10, and (d) PHA_S/PPy10 after oCVD (10 min deposition).

appearance were observed after drying, indicating the absence of detectable extractable species from the oCVD coating.

2.4. *Characterization methods*

2.4.1. *Attenuated total reflectance Fourier transform infrared spectroscopy*

FTIR spectra were recorded in the solid state using a Shimadzu ATR FTIR spectrometer. Each spectrum was collected from 4000 to 500 cm^{-1} at a resolution of 4 cm^{-1} with 64 scans averaged per sample. Prior to analysis, all samples were vacuum dried to remove residual moisture. The analysed specimens included unmodified monoliths (PHB_S, PHA_S) and monoliths coated with polypyrrole by oCVD (PHB_S/PPy5, PHB_S/PPy10, PHA_S/PPy5, PHA_S/PPy10). Spectral features were evaluated to confirm the presence of polypyrrole and to assess changes in surface chemistry after oCVD coating.

2.4.2. *Scanning electron microscopy*

Surface morphology of the porous monoliths was characterized with a Nova NanoSEM 650 (FEI, USA). Samples were mounted on carbon tape and sputter coated with a thin gold layer to enhance conductivity. Imaging was carried out under high vacuum at an accelerating voltage of 10–15 kV. Both the Everhart-Thornley detector and the through-lens detector were used in secondary electron mode, with working distances from 4.9 to 6.9 mm. Magnifications ranged from 3500 × to 6000 × to capture surface texture and pore architecture. Comparative analysis between uncoated and polypyrrole-coated monoliths was performed to evaluate coating uniformity and morphological changes. In addition, cross-sectional images of PHA_S/PPy10 were obtained by cutting the monoliths to expose internal surfaces; these cross sections were imaged under the same SEM conditions Supporting Information.

2.4.3. *Dynamic mechanical analysis*

Viscoelastic properties of neat and coated monoliths were characterized in tensile mode on a DMA Q800 instrument (TA Instruments, USA). Rectangular specimens about 5.0 mm by 8 mm by 2 mm were prepared from lyophilized samples and mounted with a gauge length of 5 mm. A temperature ramp from −100 °C to + 100 °C was applied at 3 °C min^{-1} under a constant oscillation frequency of 1 Hz and a strain amplitude within the linear viscoelastic region. The storage modulus E', loss modulus E'', and damping factor $\tan \delta = E'' / E'$ were recorded as functions of temperature. The glass transition temperature was assigned from the loss modulus (E'') peak; tan δ was used qualitatively to assess relaxation breadth. Viscoelastic parameters were compared at −40 °C, −20 °C, and 20 °C. All measurements were performed in duplicate.

2.4.4. Swelling behaviour and water contact angle

Swelling behaviour of neat and polypyrrole coated monoliths was assessed gravimetrically. Prior to analysis, all specimens were dried to constant weight at 50 °C and stored in a desiccator. Cylindrical samples of 4 mm diameter and about 2 mm height were immersed in phosphate buffered saline at pH 7.4 and 37 °C. At defined time points, samples were removed, gently blotted to remove surface liquid, and weighed. Swelling capacity was calculated as

$$\textit{Swelling capacity}(\%) = \frac{w_s - w_d}{w_d} \times 100 \tag{1}$$

where W_s is the swollen mass and W_d is the initial dry mass. Each condition was measured in triplicate and results are reported as mean ± standard deviation.

The static water contact angle of a sessile drop (3 μL) was measured by a contact angle goniometer OCA 20 (Dataphysics, Germany) equipped with SCA 21 software, where the profile was fitted with the Young–Laplace equation. At least three measurements were done at different positions of each sample, and the average value is reported.

2.4.5. Electrical conductivity

Sheet resistance of PPy coated monoliths was measured under ambient conditions using a four−point probe system (Ossila Ltd, UK, instrument range 100 mΩ/sq–10 MΩ/sq). For each sample type, three independent specimens were prepared. The average sheet resistance and standard deviation were calculated from twenty measurements per specimen and are reported in Ω/sq.

2.4.6. Antioxidant activity

Antioxidant activity was evaluated by the Trolox equivalent antioxidant capacity assay following Vostrejs et al. with minor adjustments [35]. A 7 mM ABTS solution was prepared and diluted with UV grade ethanol to an absorbance of 0.70 ± 0.02 at 734 nm. Two milliliters of this solution were added to vials containing monoliths with a surface area of about 7 mm^2 and a mass of about 40 mg. After sixty min of incubation, absorbance at 734 nm was recorded. To account for the effect of the porous matrix, the antioxidant effect of PPy coated monoliths was expressed as inhibition percentage:

$$IP(\%) = \frac{\mathrm{A}_{blank} - A_1}{\mathrm{A}_{blank}} \times 100 \tag{2}$$

where: A_{blank} is the absorbance after incubation with the uncoated monolith of the same type and A_1 is the absorbance after incubation with the coated monolith.

2.4.7. Antimicrobial activity

Antimicrobial activity was assessed using a contact-dependent broth dilution assay against the following microorganisms from the Czech Collection of Microorganisms (CCM): *Escherichia coli* (CCM 7359) and *Staphylococcus epidermidis* (CCM 4418), *Micrococcus luteus* (CCM 1569), *Serratia marcescens* (CCM 8587), and *Candida glabrata* (CCM 8270). Bacterial strains (*E. coli*, *S. epidermidis*, *M. luteus*, *S. marcescens*) were cultivated overnight in liquid medium (lysogeny broth for *E. coli*; nutrient broth for the remaining bacteria), while *C. glabrata* was cultivated in YPD medium. Cultures were grown for 24 h and standardized to 0.5 McFarland. Approximately 10 mg of sample was immersed in 1 mL of the standardized microbial suspension. After 24 h incubation at 37 °C, optical density at 600 nm (OD_{600}) was recorded. Growth inhibition was expressed as a percentage relative to the corresponding uncoated monolith of the same matrix (to isolate the contribution of the PPy coating). All experiments were performed in triplicate. This protocol corresponds to a contact-dependent broth dilution assay in liquid culture; agar diffusion tests and inhibition zones were not determined.

2.4.7.1. Resazurin metabolic activity assay (performed for Micrococcus luteus). To provide an additional viability-related endpoint for the most sensitive strain (*M. luteus*), metabolic activity after incubation with the samples was evaluated using a resazurin reduction assay. Following the 24 h contact incubation described above, aliquots of the *M. luteus* suspensions were transferred to a 96-well plate, resazurin solution was added, and the plate was incubated for 30 min at 37 °C (shaking). Absorbance was measured at 570 nm. Metabolic activity (and corresponding inhibition) was calculated relative to the appropriate growth control.

2.4.8. Cytotoxicity

Cytotoxicity was evaluated by the XTT assay according to ISO 10993–5. Mouse fibroblasts L929 (NCTC clone 929, ATCC CCL 1) were cultured in 96-well plates at 1 × 10^4 cells per well and incubated at 37 °C in a humidified atmosphere with 5 % carbon dioxide. At about 80 % confluence, cells were passaged using 0.25 % trypsin with EDTA. Extracts were prepared by incubating 0.02 g of each monolith in 0.5 mL of complete culture medium Dulbecco modified Eagle medium with 10 % fetal bovine serum and 1 % penicillin streptomycin at 37 °C for 24 h. After filtration, the extracts were applied to cell cultures and incubated for 24 h. Medium was then replaced with 50 μL per well of fresh medium containing 1 mg mL^{-1} XTT sodium salt and 7.5 μg mL^{-1} PMS. After two hours, absorbance was measured at 450 and 630 nm using a BioTek Synergy H1 microplate reader. Cell viability was expressed as a percentage relative to untreated control cells. Each condition was tested in triplicate and results are reported as mean ± standard deviation. Statistical analysis used one−way ANOVA with Tukey post hoc testing and significance at $p < 0.05$.

Cytotoxicity in direct contact was further assessed in accordance with ISO 10993–5 using embryonic mouse fibroblasts NIH/3T3 (ECACC 93061524). Cells were seeded into 12-well plates at a density of 1 × 10^5 cells per well and allowed to adhere for 24 h. After the preincubation period, the culture medium was replaced with fresh medium and square monolith samples (6 × 6 mm) were carefully placed in the centre of each well. The exposure time was 48 h. Following incubation, cells were fixed with formaldehyde, permeabilised with Triton X-100, and stained with Hoechst 33258 for nuclei and ActinRed for cytoskeletal actin filaments. Fluorescence micrographs were acquired using an Olympus IX81 inverted microscope. All tests were performed in quadruplicate.

Cell adhesion and proliferation on the material surfaces were evaluated in a separate experiment, also using NIH/3T3 fibroblasts. Cells were seeded directly onto the sample surfaces at a density of 5 × 10^4 cells cm^{-2} and cultured for 48 h. After incubation, samples were processed for fluorescence imaging using the same fixation, permeabilisation, and staining protocol as described above. Fluorescence microscopy was used to assess the presence, morphology, and spreading of cells directly on the material surfaces. All tests were performed in quadruplicate.

3. Results and discussion

3.1. Chemical and physical properties of PHB_S and PHA_S monoliths

3.1.1. Chemical structure by ATR FTIR

Successful surface modification of both porous poly(3-hydroxybutyrate) monoliths (PHB_S) and blend monoliths (PHA_S) with PPy was confirmed by ATR FTIR. Spectra of uncoated and coated monoliths are shown in Fig. 2 (PHB series) and Fig. 3 (PHA series); a reference spectrum of neat oCVD PPy on silicon is provided in Figure S1. Because the neat PPy film on silicon is much thicker and more strongly absorbing than the thin PPy coatings on the porous monoliths, its spectrum is shown separately in Figure S1 and used as a reference for band assignment rather than for direct comparison of peak intensities. Unmodified PHB_S and PHA_S display characteristic PHA absorptions, including a strong ester carbonyl near 1720 cm^{-1} , C–O stretching in the 1275–1050 cm^{-1} region, and CH_2 or CH_3 stretching around 2950–2850 cm^{-1} , consistent with the polyester backbone [12,35].

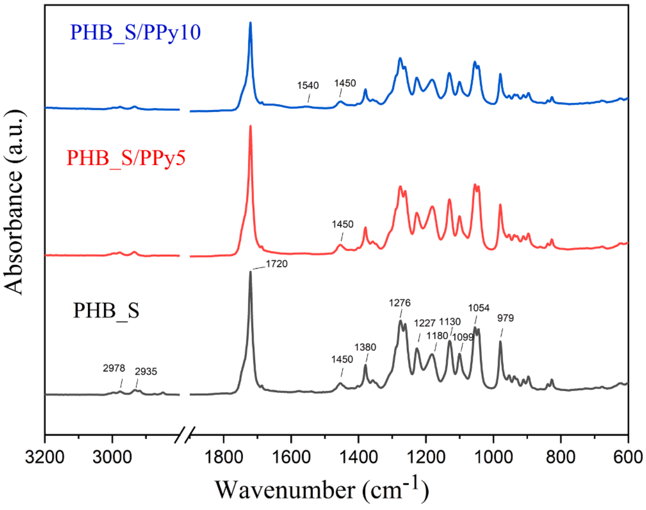

Fig. 2. ATR FTIR spectra of PHB_S and PHB_S/PPy monoliths.

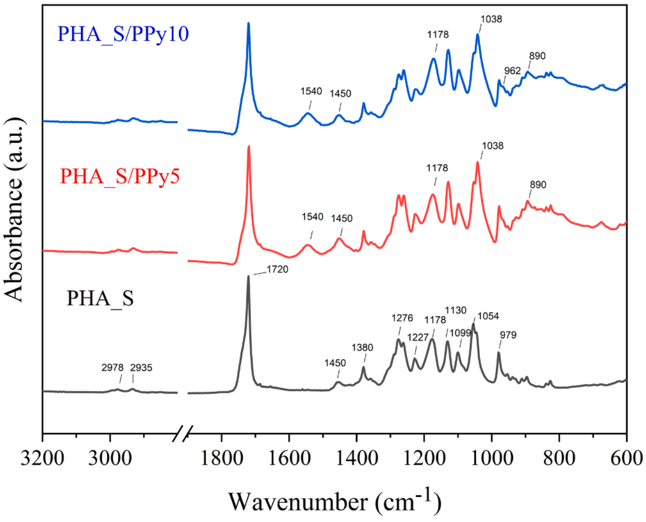

Fig. 3. ATR FTIR spectra of PHA_S and PHA_S/PPy monoliths.

After oCVD, new bands appear that are assigned to PPy. A band near 1540 cm^{-1} (ring C═C stretching) is evident in PHB_S/PPy10 but not PHB_S/PPy5, indicating that longer deposition is required for a detectable PPy signal on PHB_S within the ATR penetration depth. In contrast, the same band is distinct in both PHA_S/PPy5 and PHA_S/PPy10, consistent with more effective deposition on PHA_S even at shorter times. Increased intensity around 1450 cm^{-1} (C–N stretching) and features between ~1300 and 1000 cm^{-1} (in plane ring deformation and C–H or N–H vibrations) further support PPy presence [35]. Additional PPy associated bands marked in the PHA series (~1178, 1038, 962, and 890 cm^{-1}) strengthen with coating time (Fig. 3). Taken together, these differences point to blend composition and surface morphology in PHA_S that favour monomer and oxidant access during oCVD, producing a more uniform or thicker PPy layer, in agreement with SEM and sheet resistance trends.

3.1.2. *Surface morphology by SEM*

SEM micrographs (Fig. 4a–d) show the porous architecture typical of thermally induced phase separation [17]. PHB_S exhibits a denser structure with sporadic larger pores and lower overall porosity, whereas PHA_S presents a more regular and open network. This difference is consistent with the presence of 4-hydroxybutyrate units in the blend, which reduce crystallinity and slow solidification, allowing more time for well defined pore growth; the added chain mobility further facilitates phase separation [17–19].

After oxidative chemical vapor deposition, both monoliths show visible surface changes. PHB_S/PPy10 displays increased roughness with granular or nodular PPy deposits on pore walls, while PHA_S/PPy10 retains the open pore network with a more continuous and homogeneous PPy coverage. Regular porosity appears critical for uniform oCVD coverage and good adhesion of the conductive phase to the PHA matrix. This uniform PPy coverage improves the biointerface by increasing the effective surface area for contact based antibacterial action and by providing more accessible sites for radical scavenging (Fig. 4). Regular porosity and uniform PPy coverage also correlate with the improved rubbery plateau stiffness of PHA_S/PPy, consistent with enhanced interfacial load transfer (see Section 3.1.3 and Figures S3–S7). Cross-sectional SEM micrographs of PHA_S/PPy10 (Figure S2) further confirm that the PPy layer follows the pore walls while maintaining an interconnected porous network, in agreement with the surface views in Fig. 4.

3.1.3. *Viscoelastic properties from dynamic mechanical analysis*

Dynamic mechanical analysis captured the temperature dependent viscoelastic response of the porous monoliths across −100 to + 100 °C in tensile mode. The uncoated PHB_S monolith was mechanically unstable and not analyzable, while the PPy coating restored integrity and allowed reliable measurement. Increasing the PPy deposition time from 5 to 10 min reduced the storage modulus E′ of PHB_S/PPy over the whole temperature range, with E′ ≈ 42 MPa for PHB_S/PPy5 and ≈ 36.5 MPa for PHB_S/PPy10 at room temperature (25 °C) (Table 1). The loss modulus E″ peak shifted by about + 3.8 °C for PHB_S/PPy10 relative to PHB_S/PPy5, indicating modest restriction of molecular mobility with the thicker PPy layer. The tan δ curves were broad, consistent with multiple relaxation processes in a heterogeneous PPy modified network. We discuss E′ primarily in the 20–41 °C window as the application relevant range for wound care. Storage moduli at 20, 25, and 37 °C for all samples are summarized in Table 1; values were obtained by linear interpolation of the DMA curves (Figures S3–S7).

In contrast, the neat PHA_S monolith showed a low modulus (E′ ≈ 3.7 MPa at 25 °C) as expected for a blend containing poly(3-hydroxybutyrate-co-4-hydroxybutyrate). Deposition of PPy increased stiffness in the application relevant range, with E′ ≈ 15.2 MPa for PHA_S/PPy5 and ≈ 12.2 MPa for PHA_S/PPy10 at 25 °C (Table 1). The lower modulus for the thicker PPy layer suggests formation of more brittle PPy domains and less efficient stress transfer across the PHA PPy interface, which counteracts reinforcement. Glass transition temperatures determined from E″ were about −9.6 °C for PHA_S, −7.3 °C for PHA_S/PPy5, and −7.5 °C for PHA_S/PPy10. Together these data indicate that PPy deposition can tune stiffness in the rubbery plateau while preserving the low temperature relaxation signature of the PHA matrix.

For wound care, materials operate near 20–41 °C. In this interval the PPy coated PHA_S monoliths maintain higher E′ than the neat PHA_S, supporting handling and placement, whereas PHB_S/PPy remains stiff but without the swelling performance of PHA_S. The storage moduli of the PPy coated PHA_S monoliths are above those typical for conventional hydrogels at room temperature, which are on the order of 100 Pa to 1 MPa [36,37], and therefore fall in the high modulus hydrogel-like regime that is advantageous for mechanically supported biointerfaces (Figures S3–S7). These values are consistent with conductive biointerfaces designed for soft tissue support [5,7–11].

3.1.4. *Surface wettability and swelling behaviour*

Swelling kinetics for neat and PPy-coated porous monoliths show a biphasic profile with rapid uptake during the first hours followed by a gradual approach to equilibrium (Fig. 5). PHB_S reaches ≈ **42 %** at 24 h, consistent with hydrophobic and crystalline character of PHB. In the PHB series, PPy coating increases water uptake: PHB_S/PPy5 plateaus

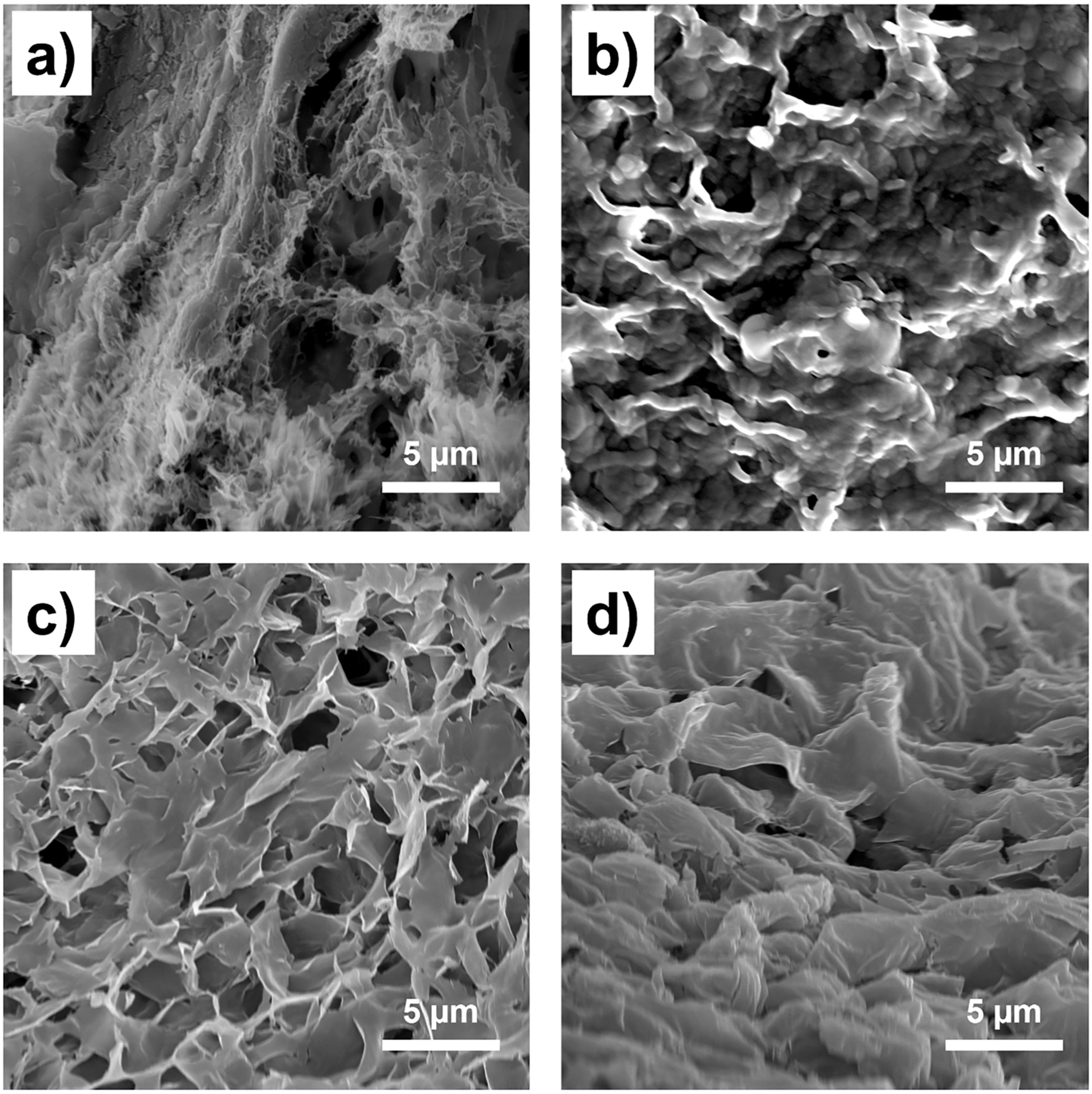

Fig. 4. SEM micrographs of monoliths: (a) PHB_S, (b) PHB_S/PPy10, (c) PHA_S, (d) PHA_S/PPy10.

Table 1

Storage modulus E' at 20, 25, and 37 °C for porous PHA and PPy-coated monoliths. Values are mean ± SD across replicate runs; otherwise representative from individual runs. Target-temperature values were obtained by linear interpolation of $E'(T)$ from the tensile DMA scans (DMA Q800, 1 Hz, 3 °C min^{-1}, −100 to +100 °C).

Sample	E' @ 20 °C (MPa)	E' @ 25 °C (MPa)	E' @ 37 °C (MPa)
PHB_S	nd	nd	nd
PHB_S/PPy5	45.7 ± 3.36	42.4 ± 1.97	32.3 ± 3.54
PHB_S/PPy10	38.3 ± 4.56	36.5 ± 2.36	31.7 ± 4.85
PHA_S	4.3 ± 0.57	3.7 ± 0.45	2.7 ± 0.32
PHA_S/PPy5	17.7 ± 0.42	15.2 ± 0.29	11.0 ± 0.05
PHA_S/PPy10	15.7 ± 12.11	12.2 ± 9.79	6.3 ± 7.76

around ≈ 69–**72 %**, whereas PHB_S/PPy10 reaches ≈ 47–**52 %**. This suggests that a thin PPy layer improves wetting and capillary ingress along pore walls, while a thicker layer partially restricts access to pores.

In the PHA series, neat PHA_S rapidly attains ≈ 220–**230 %** within ≈ 3 h and stabilizes near ≈ 270–**280 %** by 12–24 h. PPy reduces both the rate and the extent of swelling: PHA_S/PPy5 approaches ≈ 240–**250 %** by 12–24 h, while PHA_S/PPy10 levels off lower, near ≈ 160–**170 %**, with a slower rise between 12 and 24 h. The thickness dependence indicates that conformal PPy narrows effective pore entrances and adds a denser surface layer, which moderates influx and lowers the final swelling capacity. This interpretation is consistent with the SEM observations indicating a more compact surface on PPy-coated monoliths.

Taken together, PPy plays two roles that depend on the matrix. On the more hydrophobic PHB_S, a thin PPy layer improves wettability and increases swelling. On the already highly swelling PHA_S, PPy slightly suppresses uptake and slows kinetics in a thickness-dependent manner. The ≈ **270 %** capacity of PHA_S places it well within ranges reported for hydrogel−like dressings (typically about 200–**1500 %** depending on composition and microstructure), while the lower PHB_S response matches expectations for crystalline PHB [5,7,8,11]. Although the PHA_S matrix is based on hydrophobic PHA, its high apparent swelling is governed by morphology rather than by strongly hydrophilic chemistry. The thermally induced phase separation and subsequent solvent exchange create an open, interconnected porous network that becomes fully infiltrated with aqueous medium upon immersion. Thus, the gravimetric swelling ratio mainly reflects water held in the pore volume, while the P3HB/P(3HB-co-4HB) blend itself remains only moderately hydrophobic, as confirmed by water contact angles around 80 °. These results suggest a simple design guideline: regular open porosity plus a thin conformal PPy coating maximizes accessible biointerface, whereas

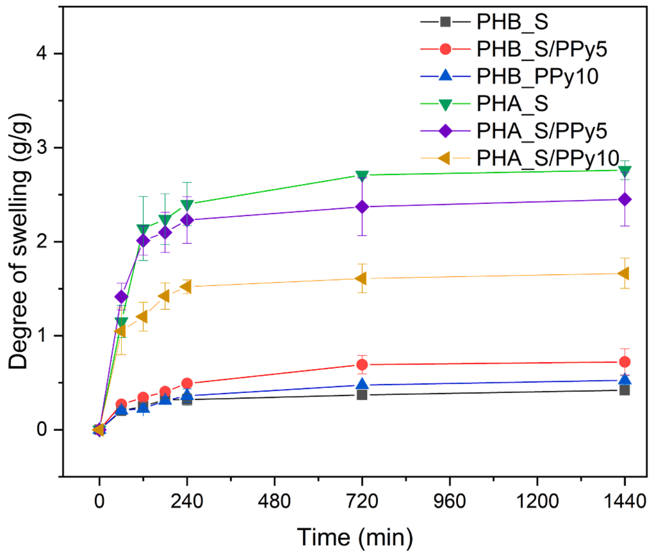

Fig. 5. Swelling kinetics of PHB_S and PHA_S monoliths with and without PPy coating (mean ± SD, n = 3).

thicker PPy reduces swelling and can hinder mass transport (Figs. 4 and 5).

To complement the swelling measurements, the surface wettability of the monoliths was assessed by static water contact angle (Table 2). Uncoated PHB_S and PHA_S showed contact angles of 79 ± 0.3 ° and 80 ± 0.4 °, respectively, which is consistent with moderately hydrophobic surfaces. PPy deposition generally reduced the contact angles of both materials, though its effect on water uptake differed between the two series. For PHB_S, a 5 min PPy coating did not appreciably change the contact angle (79 ± 0.5 ° for PHB_S/PPy5), whereas a 10 min deposition reduced it to 74 ± 0.8 ° (PHB_S/PPy10). In the PHA_S series, applying a PPy coating resulted in a stronger decrease in contact angle, from 80 ± 0.4 ° for neat PHA_S to 76 ± 0.5 ° for PHA_S/PPy5 and 71 ± 0.5 ° for PHA_S/PPy10, indicating higher surface hydrophilicity.

Although PPy increases surface hydrophilicity in both systems, the swelling response follows the trends discussed above: a thin PPy layer on PHB_S enhances swelling, whereas on PHA_S thicker PPy coatings slow water uptake and reduce the final swelling. This reduction in swelling for PHA_S is likely due to the formation of a thicker PPy layer that creates a denser outer structure and partially blocks pore entrances, thereby limiting water penetration into the monolith. This mechanistic picture is supported by SEM, which reveals a more compact surface morphology for the PPy-coated monoliths.

Table 2
Surface wettability of PHB_S and PHA_S monoliths evaluated by static water contact angle (mean ± SD).

Sample	Contact angle (°)	
PHB_S	79 ± 0.3	
PHB_S/PPy5	79 ± 0.5	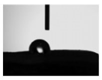
PHB_S/PPy10	74 ± 0.8	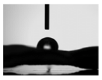
PHA_S	80 ± 0.4	
PHA_S/PPy5	76 ± 0.5	
PHA_S/PPy10	71 ± 0.5	

3.1.5. *Electrical properties*

Sheet resistance measured by the four-point probe is summarized in Table 3 (instrument range 100 mΩ per square to 10 MΩ per square; OOR denotes values above the range). PHB_S/PPy specimens showed poor conductivity, with most values out of range and only the front oriented PHB_S/PPy10 reaching about 1.9 MΩ per square. In contrast, PHA_S/PPy specimens ranged from 26 to 86 kΩ per square. Longer deposition reduced sheet resistance, consistent with thickness controlled PPy growth by oxidative chemical vapor deposition [32,33]. A clear orientation effect was observed: samples facing the oxidant and monomer streams (“front”) gave lower sheet resistance than “back” positions, in line with higher local flux and more continuous PPy pathways. These trends align with ATR FTIR and SEM, where PHB_S shows weaker PPy signatures and patchier coverage, while PHA_S exhibits uniform coating. The more hydrophilic and open porous PHA_S surface favours polypyrrole nucleation, adhesion, and continuity, which lowers sheet resistance [26,29,31].

Because film thickness inside a porous architecture is non-uniform, we report sheet resistance rather than converting to bulk conductivity. This provides a robust comparative metric across samples and conditions. These outcomes highlight the specific advantage of oxidative chemical vapor deposition on porous PHA: a solvent-free, low temperature, conformal route that preserves pore architecture while establishing continuous conducting pathways [30–33]. This mechanistic fit explains the lower sheet resistance and stronger biointerface response on PHA_S relative to PHB_S, consistent with FTIR, SEM, and antimicrobial assays. The 26–86 kΩ per square range for PHA_S/PPy is comparable to conducting polymer based dressings and coatings used for biointerfaces and is suitable for low voltage stimulation and antibacterial function [20,23–25].

3.2. *Biological properties of PHB_S and PHA_S monoliths*

3.2.1. *Antioxidant activity*

Antioxidant performance was evaluated by the Trolox equivalent antioxidant capacity method [35]. The $ABTS^{\cdot+}$ solution was adjusted to A_{734} = 0.70 ± 0.02, and each assay used monoliths of comparable exposed surface area (~7 mm^2) and mass (~40 mg). The inhibition percentage was calculated relative to the uncoated monolith of the same matrix, so the reported values isolate the contribution of the PPy layer (Fig. 6). All PPy coated monoliths showed measurable radical scavenging, consistent with the ability of polypyrrole backbones to quench $ABTS^{\cdot+}$ through electron or proton transfer [27].

Increasing deposition time from five to ten minutes increased

Table 3
Sheet resistance of PHA/PPy monoliths measured by four-point probe (mean ± SD; n = 3 specimens, 20 spots per specimen; ambient conditions). Units: kΩ/sq unless noted. OOR = out of range (≥ ~10 MΩ/sq).

Sample	Sheet resistance (kΩ/sq)
PHB_S/PPy5 (front)	OOR
PHB_S/PPy5 (back)	OOR
PHB_S/PPy10 (front)	1 993.3 ± 308.9
PHB_S/PPy10 (back)	OOR
PHA_S/PPy5 (front)	60.4 ± 0.03
PHA_S/PPy5 (back)	85.9 ± 0.06
PHA_S/PPy10 (front)	26.3 ± 0.07
PHA_S/PPy10 (back)	36.9 ± 0.04

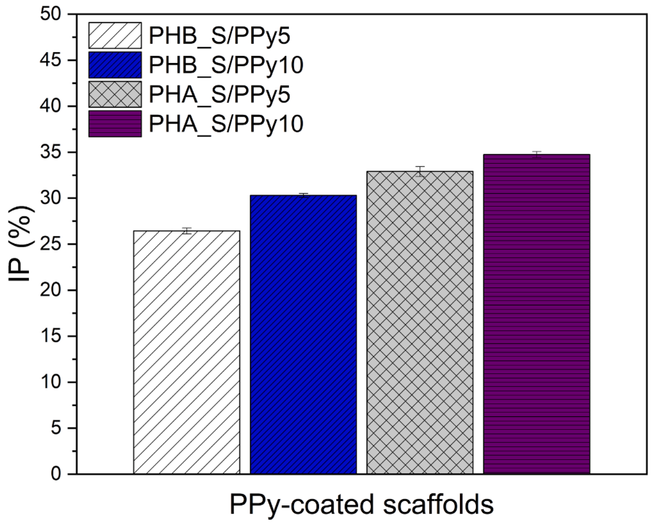

Fig. 6. Antioxidant activity of PPy coated monoliths expressed as inhibition percentage of $ABTS^{\bullet +}$ radicals.

inhibition, indicating a higher areal density of accessible redox active sites in thicker PPy. PHB_S/PPy5 and PHB_S/PPy10 reached 26.4 % and 30.3 %, while PHA_S/PPy5 and PHA_S/PPy10 reached 32.9 % and 34.7 % (means, n = 3; Fig. 6). The higher values for PHA_S/PPy mirror the ATR FTIR and SEM evidence of more uniform PPy coverage and the greater wetted surface within the open pore network, which together enlarge the effective biointerface for radical scavenging. The modest increment between five and ten min suggests that beyond a thin conformal layer, diffusion through the porous network rather than intrinsic PPy reactivity becomes rate limiting under the TEAC conditions. In line with this interpretation, samples that show higher inhibition percentages also display stronger antibacterial effects (compare Figs. 6 and 7), consistent with a common dependence on accessible PPy surface.

Mechanistically, the observed scavenging aligns with literature reports of PPy reducing $ABTS^{\cdot +}$, with activity increasing with polymer loading and continuity of the conducting phase [27]. Recent studies have demonstrated that this activity is intrinsic to the PPy structure itself and represents a critical advantage for wound healing applications. Specifically, PPy effectively scavenges ROS generated during neutrophil oxidative burst and modulates macrophage pro-inflammatory mediator production (e.g., IL-6 and NO), thereby controlling excessive inflammation that would otherwise impede the healing process. Since excessive ROS production prolongs the inflammatory phase and promotes oxidative stress-induced tissue damage, the inherent antioxidant capacity of PPy provides a dual benefit: it maintains the beneficial low-level ROS needed for microbial defense and immune cell signaling while simultaneously preventing the pathological ROS levels that compromise wound healing [26,36]. The improved biointerface created by uniform PPy coverage further contributes to the higher inhibition percentages by increasing the number of accessible radical scavenging sites.

3.2.2. *Antimicrobial activity*

The antimicrobial performance of PPy-coated porous PHA-based monoliths was assessed using a contact-dependent broth dilution assay against *Staphylococcus epidermidis*, *Escherichia coli*, *Micrococcus luteus*, *Serratia marcescens*, and the opportunistic yeast *Candida glabrata* (Fig. 7, Table S1). Uncoated monoliths did not inhibit microbial growth under the applied conditions; in several cases, negative "inhibition" values were obtained, indicating higher OD compared with the corresponding uncoated reference after baseline correction (Table S1). PPy deposition induced a clear, microorganism-dependent growth suppression, most pronounced for *M. luteus* (Fig. 7). Inhibition generally increased with coating time, particularly within the PHA_S series. For *S. epidermidis*, PHA_S/PPy10 achieved 60.6 ± 5.4 % inhibition (vs. 45.5 ± 18.3 % for PHA_S/PPy5), and for *E. coli* the same samples reached 86.9 ± 0.4 % and 83.2 ± 0.2 % inhibition, respectively (Fig. 7, Table S1).

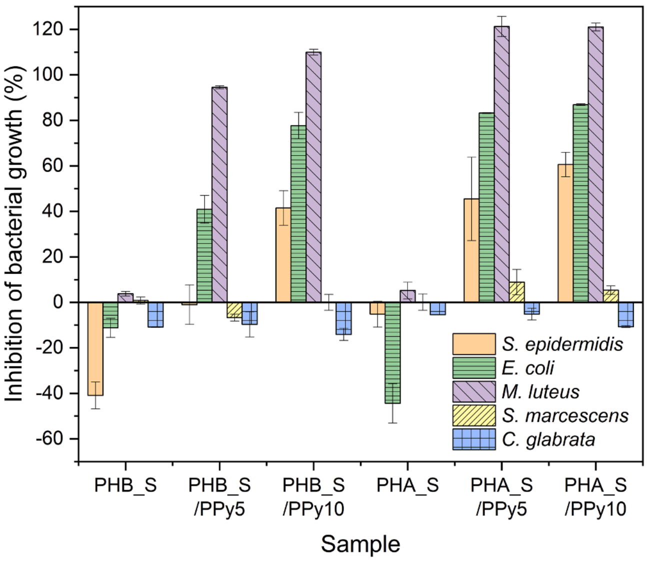

Fig. 7. Antimicrobial activity of PPy-coated monoliths after 24 h incubation with *Staphylococcus epidermidis*, *Escherichia coli*, *Micrococcus luteus*, *Serratia marcescens*, and the opportunistic yeast *Candida glabrata* in a contact-dependent broth dilution assay. Growth inhibition (%) was calculated from OD_{600} relative to the corresponding uncoated monolith of the same matrix (mean ± SD, n = 3). Negative values indicate no inhibition (OD higher than the corresponding control), and values above 100 % may arise from blank/baseline correction and correspond to complete growth suppression.

For *M. luteus*, complete growth suppression (values >100 % after blank/baseline correction, consistent with full inhibition) was observed for PHA_S/PPy5 (121.3 ± 4.5 %), PHA_S/PPy10 (121.0 ± 1.7 %), and PHB_S/PPy10 (109.9 ± 1.3 %), while PHB_S/PPy5 achieved near-complete inhibition (94.5 ± 0.6 %) (Fig. 7, Table S1).

In contrast, *S. marcescens* showed only weak inhibition across all coated samples (≤8.9 %), and *C. glabrata* remained essentially unaffected with values close to 0 % (Fig. 7, Table S1). To corroborate the strong *M. luteus* response with an independent endpoint, metabolic activity after 24 h contact incubation was quantified using a resazurin reduction assay and reported as relative metabolic activity (% of growth control) (Figure S8, Table S2). Uncoated monoliths remained comparable to the growth control (PHB_S: 106.1 ± 1.5 %; PHA_S: 106.6 ± 0.9 %). In contrast, PPy-coated samples markedly reduced bacterial metabolism (PHB_S/PPy5: 12.5 ± 5.0 %; PHB_S/PPy10: 9.7 ± 7.1 %), while PHA_S/PPy5 and PHA_S/PPy10 yielded blank-corrected values below the baseline and were therefore reported as 0 % (no detectable metabolic activity) (Figure S8, Table S2). A representative photograph of the resazurin plate together with the well allocation map is provided in Figure S9, illustrating the qualitative color response (blue: non-reduced resazurin; pink/purple: reduced resazurin) and confirming consistency between the visual endpoint and the quantitative readout. Collectively, the OD-based inhibition and resazurin assay results support a strong contact-dependent antibacterial effect of PPy-coated monoliths against *M. luteus* under the applied conditions.

The observed microorganism-dependent susceptibility aligns with prior reports on PPy-based antibacterial systems, where efficacy depends on envelope architecture and on the physicochemical state of PPy (e.g., oxidation level, counterion identity, and accessible interfacial area) [28]. In its doped/oxidized state, PPy bears a net positive charge that can promote electrostatic interactions with negatively charged microbial surfaces and thereby favour close interfacial contact [28,37]. Such adhesion is frequently discussed as a prerequisite for downstream effects that disrupt cellular homeostasis, including envelope perturbation and leakage of intracellular components [28,38].

Multiple studies further emphasize that antibacterial performance of PPy is highly morphology-dependent and is governed by how effectively the active PPy phase is presented at the microbe–material interface. Antibacterial behaviour has been linked to surface area, aggregation state, and particle/domain size, and bactericidal action has been attributed to PPy morphology in nanoparticle-based systems [38]. Aggregation can reduce the density of accessible interaction sites, whereas high-surface-area porous architectures can increase microbe–surface interactions by enabling penetration into the coated structure [28]. This framework is consistent with the present monoliths, where the stronger activity of PHA_S/PPy versus PHB_S/PPy can be rationalized by a more accessible and continuous PPy-coated surface within the porous network and improved connectivity of the conducting phase.

Controlled PPy nanoarchitectures have been reported to outperform irregular morphologies, with antibacterial performance attributed to nanostructure and dopant-dependent surface potential [39]. Related work on PPy-based cryogels likewise demonstrates that antibacterial effectiveness depends on morphology and structural integrity within hydrated porous networks, and significant activity can be achieved when PPy is appropriately integrated [29]. Oxidative chemical vapor deposition provides a route to form conformal polymer coatings on complex porous substrates, supporting formation of an accessible PPy biointerface throughout the scaffold [30]. The limited response of *S. marcescens* and *C. glabrata* is consistent with envelope structures that reduce susceptibility to contact-active interfaces: Gram-negative bacteria possess an outer membrane that can limit interactions between cationic surfaces and the cytoplasmic membrane, while yeasts present a thick, multilayered cell wall distinct from bacterial envelopes.

3.2.3. Cytocompatibility

Cytocompatibility with L929 fibroblasts after 24 h was assessed by the XTT assay in accordance with ISO 10993–5 (Fig. 8). Extracts were prepared by incubating 0.02 g of each monolith in 0.5 mL complete medium for 24 h at 37 °C, then applied to cells; viability was normalised to untreated controls (mean ± SD, n = 3; one-way ANOVA with Tukey's post hoc test, $p < 0.05$). Neat PHB_S and PHA_S were non-toxic, with cell viabilities of 84.9 ± 4.7 % and 102.2 ± 5.4 % relative to the control, respectively.

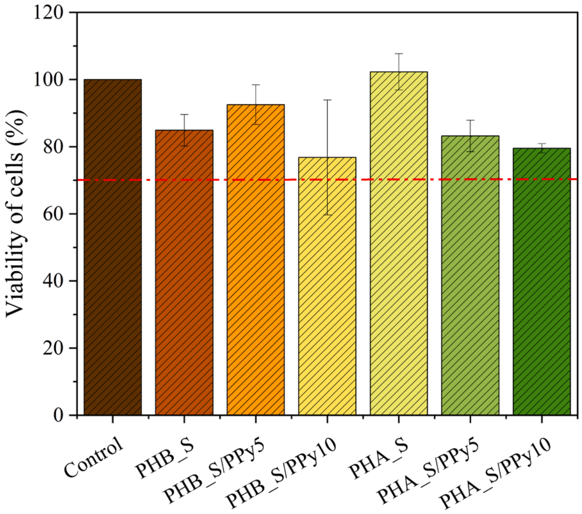

Fig. 8. Cell viability after 24 h exposure to extracts of **PHB_S** and **PHA_S** monoliths and their PPy coated counterparts, evaluated by XTT according to ISO 10993–5.

Importantly, all PPy coated monoliths except PHB_S/PPy5 remained ≥ **70 %**, meeting the ISO 10993–5 non−cytotoxicity threshold and supporting their suitability for biointerfaces. Together with the antioxidant and antibacterial results, these outcomes indicate that the PHA_S/PPy systems combine bioactivity with acceptable cytocompatibility for skin contact applications. These findings corroborate previous comprehensive studies showing that PPy exhibits low toxicity comparable to other conducting polymers, such as polyaniline [40]. Furthermore, established literature confirms that PPy biocompatibility is strongly dependent on its material form (e.g., salt vs. base, colloids vs. bulk powder) and can be effectively modulated through specific dopants [41], supporting the safety of the PPy formulation used herein.

To complement the extract-based cytocompatibility assay, the cellular response to the monoliths was also assessed in a 48 h direct-contact experiment using NIH/3T3 fibroblasts. Fluorescence staining of cell nuclei and the actin cytoskeleton showed that cells cultured in direct contact with both uncoated and PPy-coated monoliths retained their characteristic spindle-like morphology, displayed well-organised actin filaments, and formed confluent layers comparable to the tissue-culture control. No evidence of membrane damage, cytoskeletal disruption, apoptotic morphology, or impaired spreading was observed. These observations indicate that none of the tested materials exerted cytotoxic effects under direct-contact conditions, in accordance with ISO 10993–5 criteria and consistent with the extract-based viability results. Representative micrographs are provided in Fig. 9.

In contrast, cell adhesion on the material surfaces differed markedly. Fibroblasts neither attached nor proliferated on the surfaces of either neat or PPy-coated porous monoliths during the 48 h culture period, as indicated by the absence of adherent cells and the lack of cytoskeletal organisation directly on the material surfaces. This non-adhesive behaviour is attributed to the combined effects of surface chemistry and porous microstructure, which together create a low-fouling interface that does not support fibroblast attachment. From an application standpoint, such non-adhesive properties are advantageous for wound-dressing materials, where suppression of tissue ingrowth into the dressing is desirable to minimise trauma during removal and to maintain a clean interface with the wound bed. Collectively, the extract-based and direct-contact data demonstrate that the monoliths are cytocompatible while presenting a non-adhesive surface that is well aligned with their intended use as temporary wound coverings. The absence of cytotoxic effects is consistent with the solvent-free oCVD process and with the lack of detectable extractables after ethanol soaking of PPy-coated samples (Section 2.3).

4. Conclusions

This study establishes a solvent-free route to integrate hydrophobic polyhydroxyalkanoates with hydrophilic PPy by combining thermally induced phase separation with oxidative chemical vapor deposition. The process yields hydrogel−like porous monoliths that accept conformal PPy throughout the three-dimensional architecture.

Blend composition and pore regularity in PHA_S enable uniform coating, which correlates with lower sheet resistance, higher radical scavenging, and stronger antibacterial response than in PHB_S. PHA_S achieves high swelling without chemical modification, maintains cytocompatibility, and attains sheet resistance values suitable for low voltage bioelectronic use, whereas PHB_S remains brittle with limited swelling and incomplete coverage. Uniform PPy coverage strengthens the biointerface by increasing accessible surface area for contact based antibacterial action and radical scavenging.

Direct-contact assays with NIH/3T3 fibroblasts further show that these monoliths are cytocompatible yet essentially non-adhesive for fibroblasts, a combination that is advantageous for atraumatic removal of wound dressings.

Together these results demonstrate a solvent-free path to moisture−managing, mechanically resilient, and electrically functional

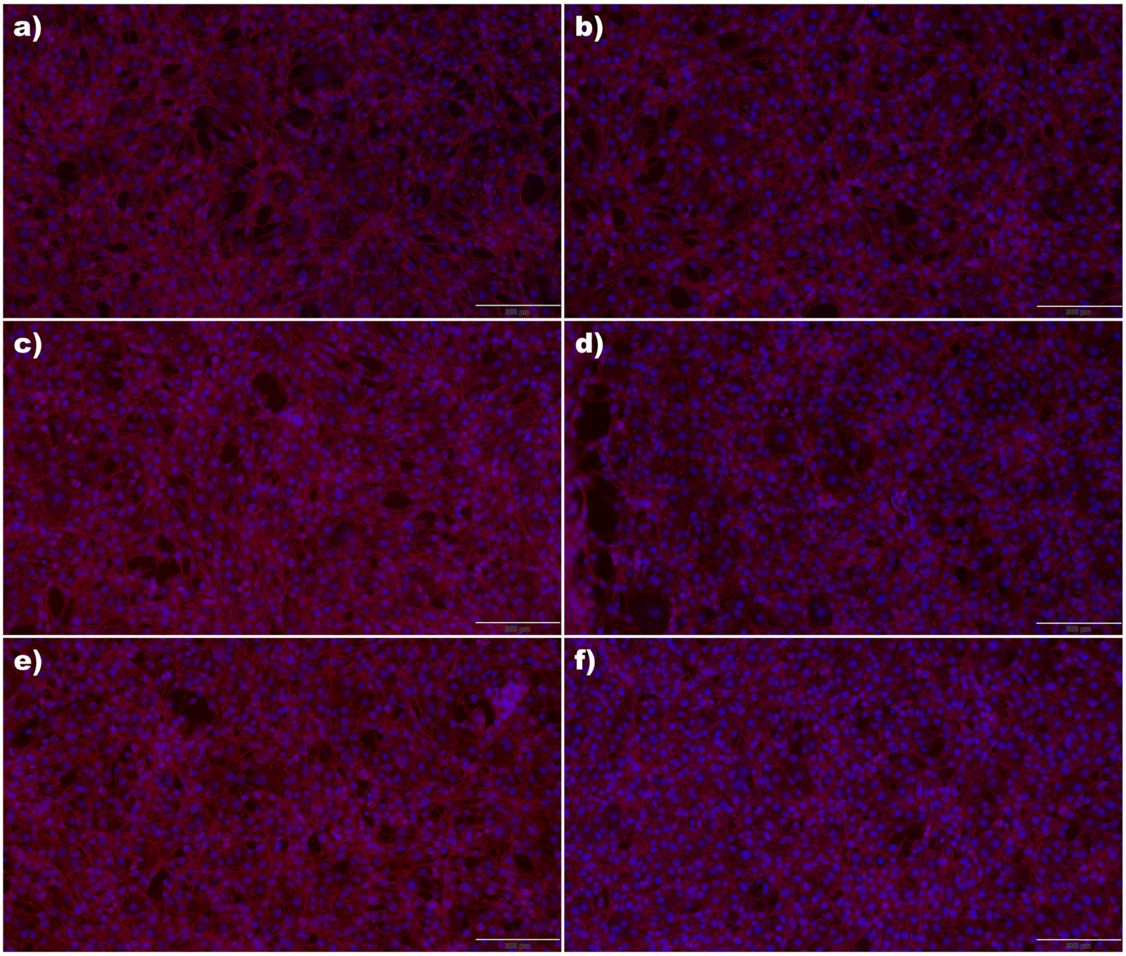

Fig. 9. Fluorescence micrographs of NIH/3T3 fibroblasts after 48 h culture on the surfaces of porous PHB_S and PHA_S monoliths and their PPy-coated counterparts. Cells were stained for nuclei (Hoechst 33258, blue) and F-actin (ActinRed, red). (a) PHB_S, (b) PHB_S/PPy5, (c) PHB_S/PPy10, (d) PHA_S, (e) PHA_S/PPy5, and (f) PHA_S/PPy10. Scale bar: 200 µm.

PHA−based dressings with intrinsic antioxidant and antibacterial activity. In this architecture the hydrophobic PHA core provides structural support and porosity for exudate management, while the conformal PPy layer defines the wound-facing biointerface by supplying conductivity for potential electrical stimulation, contact-based antibacterial action, and radical scavenging without compromising cytocompatibility. The findings support applications in bioactive and bioelectronic wound dressings and related soft tissue interfaces. Future work will quantify coating depth and uniformity in the pore network, and will assess stability during prolonged hydration at 37 °C in clinically relevant media (including cyclic wet/dry or swelling/deswelling conditions) as well as the persistence of antibacterial and antioxidant activity after sterilization and ageing; additionally, we will optimize deposition conditions and sample orientation, explore electrically controlled drug release and stimulation protocols, and extend testing to advanced antimicrobial models and in vivo wound healing.

CRediT authorship contribution statement

Adriana Kovalcik: Conceptualization; Investigation; Funding acquisition; Supervision; Validation; Writing – original draft; Writing – review & editing. **Nicole Cernekova:** Investigation. **Fika Fauzi:** Investigation. **Ranjita K. Bose:** Methodology. **Zdenko Spitalsky:** Investigation. **Zuzana Kadlecova:** Investigation. **Lucy Vojtova:** Methodology. **Zdenka Víchová:** Investigation; Methodology. **Petr Humpolíček:** Investigation; Methodology. **Patrycja Bober:** Conceptualization; Supervision.

Declaration of Competing Interest

The authors declare that they have no known competing financial interests or personal relationships that could have appeared to influence the work reported in this paper.

Acknowledgements

This study was funded by the project GA 25–15806S of the Czech Science Foundation (GACR). Additionally, Nicole Cernekova was supported by the Erasmus+ mobility program (101/2024–2025), which enabled her research stay at the University of Groningen.

Appendix A. Supporting information

Supplementary data associated with this article can be found in the online version at doi:10.1016/j.colsurfb.2026.115417.

Data availability

Data will be made available on request.

References

[1] VVSR Karri, G. Kuppusamy, SV Talluri, K. Yamjala, SS Mannemala, Ramanjaneyulu G. Current and emerging therapies in the management of diabetic foot ulcers, Curr. Med. Res. Opin. 32 (2016) 519–542, https://doi.org/10.1185/03007995.2015.1128888.

[2] MG Monaghan, R. Borah, C. Thomsen, S. Browne, Thou shall not heal: overcoming the non-healing behaviour of diabetic foot ulcers by engineering the inflammatory microenvironment, Adv. Drug Deliv. Rev. 203 (2023) 115120, https://doi.org/10.1016/j.addr.2023.115120.

[3] P. Norton, P. Trus, F. Wang, MJ Thornton, C. Chang, Understanding and treating diabetic foot ulcers, Ski. Health Dis. 4 (2024) e399, https://doi.org/10.1002/ski2.399.

[4] S. Zhao, X. Hu, Y. Zhao, et al., Hydrogel-based therapies for diabetic foot ulcers, Burns Trauma 13 (2024) tkae084, https://doi.org/10.1093/burnst/tkae084.

[5] DA Gyles, LD Castro, JOCS Júnior, RM. Ribeiro-Costa, A review of the designs and prominent biomedical advances of natural and synthetic hydrogel formulations, Eur. Polym. J. 88 (2017) 373–392, https://doi.org/10.1016/j.eurpolymj.2017.01.027.

[6] H. Geckil, F. Xu, X. Zhang, S. Moon, U. Demirci, Engineering hydrogels as extracellular matrix mimics, Nanomedicine 5 (2010) 469–484, https://doi.org/10.2217/nnm.10.12.

[7] AS. Hoffman, Hydrogels for biomedical applications, Adv. Drug Deliv. Rev. 64 (2012) 18–23, https://doi.org/10.1016/j.addr.2012.09.010.

[8] D. Caccavo, S. Cascone, G. Lamberti, AA. Barba, Hydrogels: Experimental characterization and mathematical modelling of mechanical and diffusive behaviour, Chem. Soc. Rev. 47 (2018) 2357–2373, https://doi.org/10.1039/C7CS00638A.

[9] X. Zhao, X. Chen, H. Yuk, S. Lin, X. Liu, GA. Parada, Soft materials by design: Unconventional polymer networks give extreme properties, Chem. Rev. 121 (2021) 4309–4372, https://doi.org/10.1021/acs.chemrev.0c01088.

[10] Q. Chen, H. Chen, L. Zhu, J. Zheng, Fundamentals of double network hydrogels, J. Mater. Chem. B. 3 (2015) 3654–3676, https://doi.org/10.1039/C5TB00123D.

[11] Y. Teng, J. Chi, J. Huang, et al., Hydrogel toughening resets biomedical application boundaries, Prog. Polym. Sci. 161 (2025) 101929, https://doi.org/10.1016/j.progpolymsci.2025.101929.

[12] The Handbook of Polyhydroxyalkanoates, CRC Press, Boca Raton, FL, 2020, https://doi.org/10.1201/9781003080718.

[13] E. Elmowafy, A. Abdal-Hay, A. Skouras, M. Tiboni, L. Casettari, V. Guarino, Polyhydroxyalkanoate applications in drug delivery and tissue engineering, Expert Rev. Med. Devices 16 (2019) 467–482, https://doi.org/10.1080/17434440.2019.1615439.

[14] L. Kaniuk, U. Stachewicz, Development and advantages of biodegradable PHA polymers based on electrospun PHBV fibers, ACS Biomater. Sci. Eng. 7 (2021) 5339–5362, https://doi.org/10.1021/acsbiomaterials.1c00757.

[15] L. Brelle, F. Faÿ, T. Ozturk, et al., Hydrogel based on polyhydroxyalkanoate sulfonate, Biomacromolecules 24 (2023) 1871–1883, https://doi.org/10.1021/acs.biomac.3c00059.

[16] V. Sharma, R. Sehgal, R. Gupta, Polyhydroxyalkanoate: Properties and modifications, Polymer 212 (2021) 123161, https://doi.org/10.1016/j.polymer.2020.123161.

[17] T. Tsujimoto, N. Hosoda, H. Uyama, Fabrication of porous poly(3-hydroxybutyrate-co-3-hydroxyhexanoate) monoliths via thermally induced phase separation, Polymers 8 (2016) 66, https://doi.org/10.3390/polym8030066.

[18] C.-K. Kang, S. Kusaka, Y. Doi, Structure and properties of poly(3-hydroxybutyrate-co-4-hydroxybutyrate) produced by Alcaligenes latus, Biotechnol. Lett. 17 (1995) 583–588, https://doi.org/10.1007/BF00129382.

[19] A. Kovalcik, J. Smilek, M. Machovsky, et al., Properties and structure of poly(3-hydroxybutyrate-co-4-hydroxybutyrate) filaments for fused deposition modelling, Int. J. Biol. Macromol. 183 (2021) 880–889, https://doi.org/10.1016/j.ijbiomac.2021.04.183.

[20] AA Kohestani, Z. Xu, FE Baştan, AR Boccaccini, F. Pishbin, Electrically conductive coatings in tissue engineering, Acta Biomater. 186 (2024) 30–62, https://doi.org/10.1016/j.actbio.2024.08.007.

[21] U. Riaz, N. Singh, F. Srambikal, S. Fatima, A review on synthesis and applications of polyaniline and polypyrrole hydrogels, Polym. Bull. 80 (2023) 1085–1112, https://doi.org/10.1007/s00289-022-04120-6.

[22] JH Collier, JP Camp, TW Hudson, CE. Schmidt, Polypyrrole–hyaluronic acid composite biomaterials, J. Biomed. Mater. Res. 50 (2000) 574–584, https://doi.org/10.1002/(SICI)1097-4636(20000615)50:4.

[23] Y. Li, Wan P. Dong, Y. Fan, B. Qian, W. Ji, X. Lu, X. Gan, D. Liu, P. PEDOT incorporated gelatin based conductive hydrogel for wound healing in vitro, ACS Appl. Polym. Mater. 5 (2023) 4233–4245, https://doi.org/10.1021/acsapm.3c00445.

[24] S. Liu, D. Li, Y. Wang, G. Zhou, K. Ge, L. Jiang, D.PVA Fang, MXene polyaniline hydrogel enhancing skin wound healing, Biomater. Sci. 10 (2022) 3585–3598, https://doi.org/10.1039/D2BM00575A.

[25] S. Wang, L. Yuan, Z. Xu, X. Lin, L. Ge, D. Li, Mu, Ch. Functionalization of an electroactive self-healing polypyrrole-grafted gelatin hydrogel by incorporating a polydopamine@AgNP nanocomposite, ACS Appl. Bio Mater. 4 (2021) 5321–5333, https://doi.org/10.1021/acsabm.1c00548.

[26] S. Káčerová, Z. Víchová, K. Valášková, J. Vícha, L. Münster, V. Kašpárková, O. Vašíček, P. Humpolíček, Biocompatibility of colloidal polypyrrole, Colloids Surf. B Biointerfaces 232 (2023) 113605, https://doi.org/10.1016/j.colsurfb.2023.113605.

[27] CF Hsu, H. Peng, C. Basle, J. Travaš-Sejdić, PA. Kilmartin, ABTS•+ scavenging activity of polypyrrole, polyaniline and PEDOT, Polym. Int. 60 (2010) 69–77, https://doi.org/10.1002/pi.2912.

[28] FAG da Silva, SA Vieira, S.de Á Botton, MM da Costa, HP de Oliveira, Antibacterial activity of polypyrrole based nanocomposites, Pol. ímeros 30 (2020) e2020049, https://doi.org/10.1590/0104-1428.08020.

[29] KA Milakin, Z. Capáková, U. Acharya, J. Vajďák, Z. Morávková, J. Hodan, P. Humpolíček, P. Bober, Biocompatible and antibacterial gelatin based polypyrrole cryogels, Polymer 197 (2020) 122491, https://doi.org/10.1016/j.polymer.2020.122491.

[30] WE Tenhaeff, KK. Gleason, Initiated and oxidative chemical vapor deposition of polymeric thin films, Adv. Funct. Mater. 18 (2008) 979–992, https://doi.org/10.1002/adfm.200701479.

[31] F. Fauzi, RK. Bose, Mechanistic study of oxidative chemical vapor deposition of polypyrrole: Effects of the inert gas and deposition time, Appl. Surf. Sci. Adv. 25 (2024) 100673, https://doi.org/10.1016/j.apsadv.2024.100673.

[32] A. Dianatdar, M. Miola, O. Di Luca, P. Rudolf, F. Picchioni, RK. Bose, All dry one step synthesis, doping, and film formation of conductive polypyrrole, J. Mater. Chem. C. 10 (2021) 557–566, https://doi.org/10.1039/D1TC05082F.

[33] F. Fauzi, Y. Di, DM Morales, RK. Bose, Supercapacitive behavior of oxidative chemical vapor deposited polypyrrole on carbon fabric in aqueous electrolytes, ACS Appl. Energy Mater. 8 (2025) 4656–4668, https://doi.org/10.1021/acsaem.5c00283.

[34] A. Mukherjee, J. Es Sayed, B. Corci, J. Suyanto, A. van der Molen, AM Dolga, AGP Kottapalli, M. Kamperman, RK. Bose, Soft on tissue, strong on signal: enabling tissue compatible pressure sensing conductive hydrogels via oxidative chemical vapor deposition, Mater. Today Chem. 49 (2025) 103085, https://doi.org/10.1016/j.mtchem.2025.103085.

[35] P. Vostrejs, D. Adamcová, MD Vaverková, et al., Active biodegradable packaging films modified with grape seeds lignin, RSC Adv. 10 (2020) 29202–29213, https://doi.org/10.1039/D0RA04074F.

[36] S. Káčerová, M. Muchová, H. Doudová, L. Münster, B. Hanulíková, K. Valášková, V. Kašpárková, I. Kuřitka, P. Humpolíček, Z. Víchová, O. Vašíček, J. Vícha, Chitosan/dialdehyde cellulose hydrogels with covalently anchored polypyrrole: novel conductive, antibacterial, antioxidant, immunomodulatory, and anti-inflammatory materials, Carbohydr. Polym. 327 (2024) 121640, https://doi.org/10.1016/j.carbpol.2023.121640.

[37] DO Sanchez Ramirez, A. Varesano, RA Carletto, C. Vineis, I. Perelshtein, M. Natan, N. Perkas, E. Banin, A. Gedanken, Antibacterial properties of polypyrrole-treated fabrics by ultrasound deposition, Mater. Sci. Eng. C. 102 (2019) 164–170, https://doi.org/10.1016/j.msec.2019.04.016.

[38] FAG da Silva Jr, et al., Antibacterial behavior of polypyrrole: the influence of morphology and additives incorporation, Mater. Sci. Eng. C. 62 (2016) 317–322, https://doi.org/10.1016/j.msec.2016.01.067.

[39] S. Golba, J. Loskot, The alphabet of nanostructured polypyrrole, Materials 16 (22) (2023) 7069, https://doi.org/10.3390/ma16227069.

[40] P. Humpolíček, V. Kašpárková, J. Pacherník, J. Stejskal, P. Bober, Z. Capáková, KA Radaszkiewicz, I. Junkar, M. Lehocký, The biocompatibility of polyaniline and polypyrrole: a comparative study of their cytotoxicity, embryotoxicity and impurity profile, Mater. Sci. Eng. C. 91 (2018) 303–310, https://doi.org/10.1016/j.msec.2018.05.037.

[41] Z. Capáková, KA Radaszkiewicz, U. Acharya, TH Truong, J. Pacherník, P. Bober, V. Kašpárková, J. Stejskal, J. Pfleger, M. Lehocký, P. Humpolíček, The biocompatibility of polyaniline and polypyrrole 2: doping with organic phosphonates, Mater. Sci. Eng. C. 113 (2020) 110986, https://doi.org/10.1016/j.msec.2020.110986.